NANOSYSTEMS:
PHYSICS, CHEMISTRY, MATHEMATICS

Sarma R., et al. *Nanosystems: Phys. Chem. Math.*, 2022, **13** (5), 546–564.
http://nanojournal.ifmo.ru
DOI 10.17586/2220-8054-2022-13-5-546-564

Original article

Synthesis and optical properties of MnSe nanostructures: A review

Runjun Sarma[1,a], Munmi Sarma[2], Manash Jyoti Kashyap[3,b]

[1]Mehr Chand Mahajan DAV College for Women, Sector 36, Chandigarh, India

[2]Sensors & Biosensors group, Autonomous University of Barcelona, Spain

[3]Polymer Technology Consultant, Chandigarh, India

[a]runjun2018chd@gmail.com, [b]manashjk@gmail.com

Corresponding author: Runjun Sarma, runjun2018chd@gmail.com

ABSTRACT Manganese selenide is an important diluted magnetic semiconductor (DMS) material having both optical and magnetic properties especially in the nanometer scale. Because of the phenomena of polymorphism exhibited by MnSe, it can be an interesting material for controlled polymorphism synthesis by using different synthesis procedures. In this review article, we discuss various synthesis procedures (wet chemical and deposition methods) of different MnSe nanostructures and their optical properties. The dependence of various optical properties (UV-Vis spectroscopy, photoluminescence spectroscopy and time resolved photoluminescence spectroscopy) of the MnSe nanostructures on the methods of synthesis is discussed in this article. We are specially focused on the reaction parameters of synthesis process that influence on the optical properties of the MnSe nanostructures. Moreover, the Stokes shift is calculated for the MnSe nanostructures synthesized by different procedures. Large Stokes shifts observed for MnSe nanostructures create a promising potentials in various applications including multiplex assay, bio-imaging, bio-sensing etc.

KEYWORDS diluted magnetic semiconductor, chalcogenides, stokes shift, wet chemical methods, deposition methods

FOR CITATION Sarma R., Sarma M., Kashyap M.J. Synthesis and optical properties of MnSe nanostructures: A review. *Nanosystems: Phys. Chem. Math.*, 2022, **13** (5), 546–564.

1. Introduction

Diluted magnetic semiconductors (DMS) known as semi-magnetic semiconductors are a new class of materials which is prepared by doping a host material commonly chosen from amongst II–VI, III–VI, IV–VI group semiconductor materials with a small concentration (< 10 %) of magnetic ions of transition metals [1–4]. Substitutional magnetic atoms such as Mn, Co, Fe, etc., make up a part of the lattices of the host material. The combinations of magnetic and non-magnetic materials lead to the co-existence of both magnetic and semiconducting properties in the alloyed DMS. The most extensively studied and most thoroughly described materials of this type are the $A^{II}_{1-x}Mn_xB^{VI}$ alloys in which a fraction of the cation sites of the host semiconductor are replaced by manganese ions [2,5,6]. In manganese dopped II-VI semiconductors, as the valency (+2) of Mn atoms is the same as that of cations of the host material, Mn^{2+} ions can be easily incorporated in the cationic sites. DMS of $A^{II}_{1-x}Mn_xB^{VI}$ type are of interest for several distinct reasons. Their ternary nature opens up the possibility of "tuning" the lattice constant and band parameters by varying the concentration of Mn atoms. Furthermore, the presence of localized magnetic ions in these semiconductor alloys leads to an exchange interaction between the *sp* band electrons of the host semiconductor and the *d* orbital electrons associated with Mn^{2+} ion. This results in extremely large Zeeman splitting (order of tens of meV) of electronic band structures providing diverse magneto-optical effects [7,8]. There are various applications in which the DMS are widely used, such as in the production of LEDs [9], spin transistors [10] capacitors [11], biological imaging [12], etc.

Manganese selenide belongs to the group of chalcogenides and are essentially binary-semiconductor systems denoted by $Zn_{1-x}Mn_xSe$ where x equals 1 and, correspondingly, is a member of the family of these magnetic semiconductors signified by the absence of zinc (Zn_{1-1}). Manganese selenide can be found in nature as three polymorphs: i) two cubic modified α-MnSe, existing as a rock salt structure (RS) and β-MnSe existing as zinc blende (ZB) [13], and ii) hexagonally modified wurtzite structure (WZ), existing as γ-MnSe [14, 15]. In α-MnSe, selenium (Se^{2-}) anions are expanded in FCC lattice arrangements while Mn^{2+} ions occupy the octahedral sites. In β-MnSe, though the Se^{2-} anions are expanded in FCC lattice arrangements, the Mn^{2+} ions are located in half of the tetrahedral sites. γ-MnSe crystal structures comprises HCP lattice of Se^2 ions with half of the tetrahedral sites occupied by the Mn^{2+} ions. Fig. 1 shows schematic diagram of a crystal of three polymorphs of MnSe.

The polymorphic forms of MnSe differ in their stability of existence. While the octahedrally coordinated rock salt structure of cubic modified α-MnSe is naturally stable, the β-MnSe existing as ZB and γ-MnSe existing as WZ are found to be metastable [15, 16]. Moreover, these polymorphic forms can be differentiated by their distinct magnetic

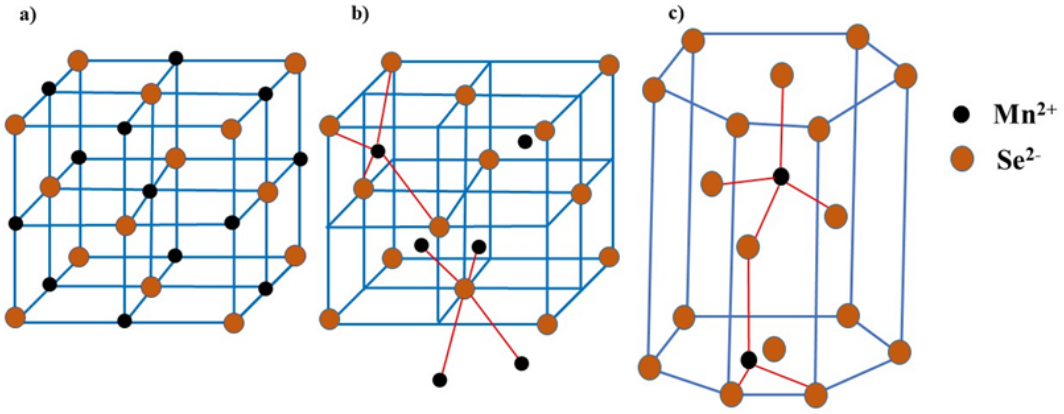

FIG. 1. Schematic diagram (not to scale) of cubic modified a) α-MnSe; b) β-MnSe and hexagonally modified; c) γ-MnSe crystal structure

behavior. While α-MnSe is antiferromagnetic [17] in nature, β-MnSe and γ-MnSe primarily exhibit ferromagnetic characteristics [18]. The γ-MnSe structures in spite of their instability are of significant interest due to their structural compatibility with semiconductor systems belonging to the II–VI groups that exhibit elevated fluorescent and photostable properties [19]. The fluorescent behavior [20,21], and magnetic response [22] characteristics of MnSe nanostructures can be collaboratively utilized in new applications requiring coordination of bright-fluorescent imaging in the presence of an externally applied magnetic field.

Amongst highly fluorescent semiconductor systems, Cd-based chalcogenide ones i.e., CdSe [23], CdTe [24], CdS [25], and CdSe/ZnS core-shell QDs [26] have attracted the maximum attention in biophysical research; particularly as tagging, labeling, and imaging agents. This takes place because of their unique properties such as large band gap tunability, bright emission response, high photostability, high quantum yield, narrow emission as well as wide absorption bands etc. [27,28]. Nevertheless, biocompatible nature of these QDs in cellular environments and under UV illumination remains questionable owing to the high toxicity level of free Cd, thereby limiting applications in nano-biotechnology and bioengineering fields are possible [29, 30]. Since energy of the UV radiation is close to the chemical bond energy, there is a possibility of a process similar to photolytic dissolution releasing toxic heavy metal ions of Cd^{2+}. Replacing Cd by Mn (for instance, choosing MnS and MnSe instead of CdS and CdSe) would help one in reducing the toxicity level by avoiding the photobleaching of Mn^{2+} [31–34]. Knowing that, Mn^{2+} precursor is a hard Lewis acid [32, 35] while Cd^{2+} precursor is a relatively softer one, the former is less reactive to the surrounding thus experiencing much lowered photobleaching as compared to the latter [32].

In this review article, we are focused on synthesis procedures of different MnSe nanostructures and their optical properties. Several bottom-up approaches ranging from wet chemical methods to vapor deposition methods used for the synthesis of MnSe nanostructures are summarized here. Moreover, variation of optical properties due to the methods of synthesis are discussed in the article. While discussing this behavior, various reaction parameters affecting their optical properties are also included.

2. Various synthesis procedures of MnSe nanostructures

Till now, a large number of synthesis methods have been developed for the preparation of MnSe nanostructures. The choice of an appropriate method of synthesis of nanostructures depends mainly on the targeted application and the technology involved. Various synthesis routes have their limitations but the choice of the most convenient method for preparation of nanostructures is influenced by the advantages or otherwise, encountered on account of different reaction conditions and the precursor or starting materials used. MnSe nanostructures can be synthesized by using various wet chemical and deposition methods. We discuss below different methods that are used for synthesizing MnSe nanostructures as reported by various research groups.

2.1. Wet chemical methods

Wet chemical methods are commonly used synthesis procedures where liquid dispersing media is used at one of the stages of the synthesis process. Hydrothermal, solvothermal and hot injection methods are various wet chemical methods that have been used for the synthesis of differently shaped crystalline MnSe nanostructures.

2.1.1. Hydrothermal method. Hydrothermal method is one of the simplest, environmentally friendly, cost-effective techniques for synthesis of various nanostructures. In spite of the low cost and simplicity, this process has various other advantages including i) highly controlled production of the nanostructures in terms of morphology, composition, structure etc., ii) fast reaction kinetics, iii) phase purity, iv) high crystallinity, v) narrow particle-size distributions etc. Water is used

as the main reaction medium in the hydrothermal synthesis process. The precursors and the other reacting materials to be used for a particular synthesis process are dissolved in water in a sealed autoclave vessel coated with Teflon layer. The reacting materials inside the autoclave are kept at a moderate temperature (usually higher than the boiling point of solvent, i.e., > 100 °C) for a period of time (depending on the morphology and size) at a very high pressure. Fig. 2(a) depicts the schematic diagram of hydrothermal synthesis process.

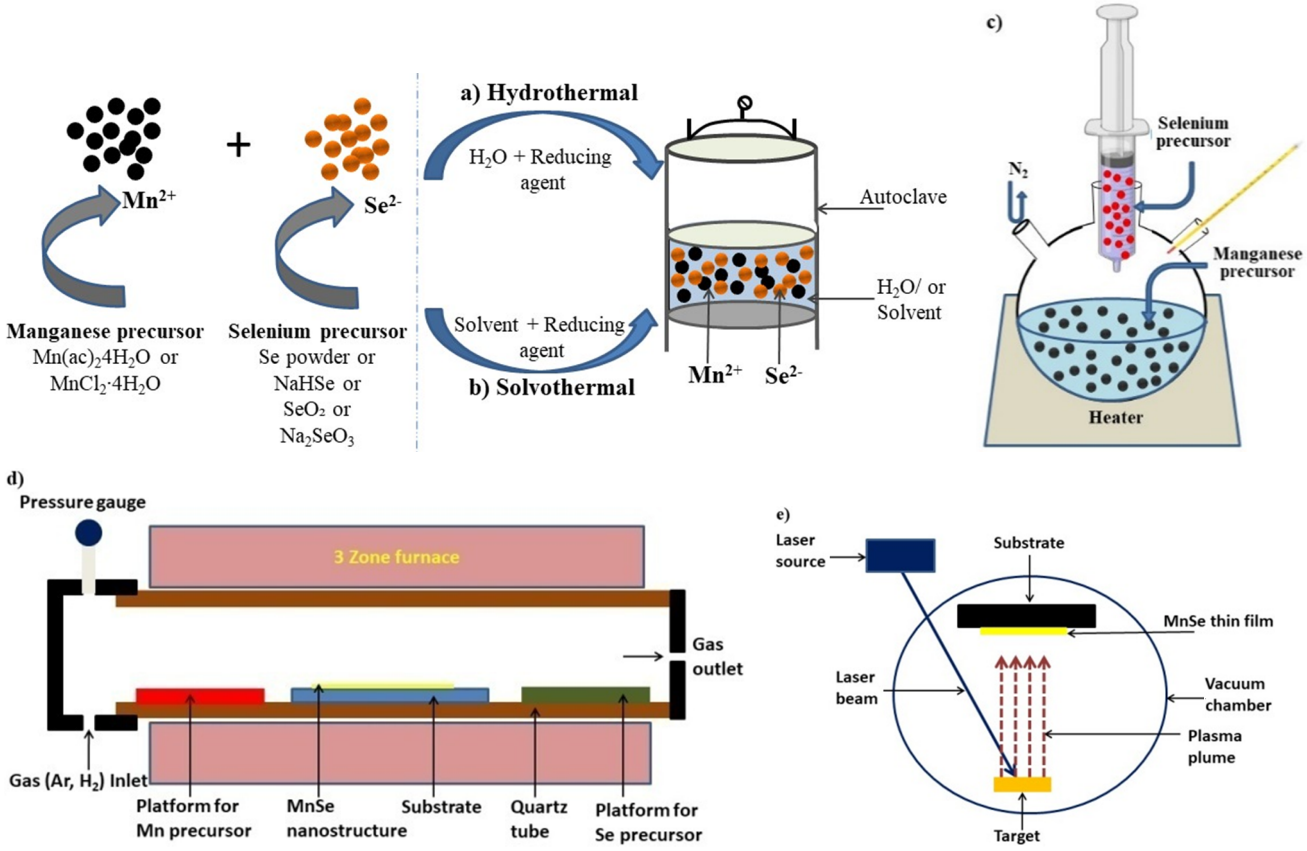

FIG. 2. Schematic diagram of various synthesis methods: a) hydrothermal; b) solvothermal; c) hot injection; d) chemical vapor deposition; e) pulsed laser deposition discussed in the article for the synthesis of MnSe nanostructures

The first hydrothermal synthesis of α-MnSe in the form of nanorods was believed to be carried out via the reaction of aqueous alkaline Se powder (selenium precursor) with manganese acetate tetrahydrate ($Mn(CH_3COO)_2 \cdot 4H_2O$) (manganese precursor) in the presence of the reducing agent hydrazine hydrate. The reaction was carried out in the reaction temperature range of 100 – 180 °C for 12 h in a stainless-steel autoclave coated with Teflon layer. The research group used the hydrothermal synthesis procedure to study the effect of precursor concentration, time and temperature on the formation of MnSe. The pure phase of MnSe was found to be synthesized at a temperature of 180 °C and reaction time 6 h. Below 180 °C a combined phase of $MnSe_2$ and MnSe was obtained. Morphologically different MnSe structures were obtained by varying the Se^{2-} ion concentration (in the reaction mixture) and controlling the reaction temperature [36]. In the presence of alkaline solution such as NaOH, commercially available Se powder dissolves to form Se^{2-} and SeO_3^{2-} ions in the reaction mixture on account of the formation and subsequent dissociation of Na_2Se and Na_2SeO_3. At low temperatures, SeO_3^{2-} reduces to elemental Se which is highly reactive as compared to the commercially available Se powder. Finally, this results in the production of Se^{2-} via deprotonation in alkaline condition. At high temperature (~ 180 °C), largely available Se^{2-} concentrations, hinders the Se formation from SeO_3^{2-} which is responsible for forming of cubic sized nanocrystals. This results in higher driving force for the formation of rod structured nano MnSe compared to cubic structured. Whereas at the low temperature (~ 100 °C), favorable condition (ideal Se^{2-} concentrations and Se formation) for the production of cubic shaped nano MnSe can be obtained [36].

A simpler hydrothermal method (a modification of the traditional hydrothermal method) can be used to synthesize monodisperse α-MnSe rod like nanoparticles having average base diameter of 100 nm and tip diameter of 20 nm. In this method, sodium borohydride with reduced elemental selenium reacts with manganese precursor to produce MnSe nanorods by stirring at a low temperature of 40 °C for 60 minutes instead of using high temperature of 180 °C for 12 h at high pressure typical in hydrothermal synthesis methods [37].

Water solubility, biological stability, biocompatibility in MnSe QDs can be achieved by the use of coating (capping) agents/ligand molecules/surfactants in the hydrothermal synthesis method. However, depending on the chemistry and structure of these surface functionalized materials, the average size of the MnSe QDs significantly varies. Water solubility of MnSe nanoparticles have been achieved by using agents like Thioglycolic acid (TGA) and Sodium dodecyl sulfate (SDS) in the synthesis process. Amphiphilic ligands use their non polar part as a binding intermediate with the nanoparticle and the polar or hydrophilic groups on the other end ensures the water solubility of the same. The use of TGA molecules have led to the formation of spherically shaped, wurtzite (WZ) phase MnSe QDs of average size 5 nm. Substitution of TGA molecules with SDS surfactant in the synthesis of MnSe led to larger sized (~ 14 nm) QDs. The apparent difference in the sizes of the QDs produced by TGA and SDS routes in the hydrothermal method can be attributed to the short chained and long chain characteristics of TGA and SDS respectively [38]. Similarly, α-MnSe QDs with sizes in the range of 5 to 11 nm can be obtained by using different capping agents such as cetyltrimethyl ammonium bromide (CTAB), TGA and dextran around the QDs while keeping other reaction parameters constant [39].

The size of the hydrothermally synthesized MnSe nanostructures was found to be pH dependent. With change of pH effective net charge on the surface of the nanostructure in the suspension changes which results in the formation of nanostructures of different size. Hexagonally shaped α-MnSe nanodisc was synthesized by using the hydrothermal method with an increase in size from nanoscale to microscale by variation of pH value from 6 to 10 [40]. In contrast, spherical shaped MnSe QDs experienced decrease in hydrodynamic size (overall size of the particles covered by water molecules) from 46.5 to 20.3 nm with increasing pH of reacting medium from 2.5 to 9 [41].

The hydrothermal method was used to synthesize α-MnSe nanoparticles of size in the range of 20 to 30 nm that was used to form a pseudocapacitive electrode material for supercapacitor [42]. Similarly, hydrothermally synthesized MnSe multilayered structures were formed by small quantities of microplates surrounded by many numbers of nanoplates were used to improve the performance of electrochemical energy storage devices [43]. Table 1 summarizes the data of MnSe nanostructures synthesized by hydrothermal method.

2.1.2. Solvothermal method. Solvothermal method is similar to the hydrothermal method used for the synthesis of various nanostructures. The mediums that can be used in solvothermal synthesis processes can be organic or inorganic solvents with high boiling point; but not water. The use of solvents offers high diffusivity, increased mobility of the dissolved ions thus allowing better mixing of the reagents. Moreover, the density, viscosity, and the molecular structure of solvents may strongly influence the properties of the final product. Similar to the hydrothermal method, chemical reactions in the solvothermal method are conducted in sealed autoclaves by heating both precursor and the solvent at high pressure and temperatures [44]. In this method, the autoclave is maintained at a temperature higher than the boiling temperature of the solvent. In spite of having other advantages as similar to hydrothermal method, another important advantage of the solvothermal method is that any material can be dissolved in the solvent by increasing the temperature and pressure to the critical points of the solvent. Fig. 2(b) depicts the schematic diagram of solvothermal synthesis process.

Solvothermal method was used for the synthesis of highly crystalline α-MnSe nanostructures in nitrogen containing solvent ethylenediamine (en) by using $MnCl_2 \cdot 4H_2O$ and selenium (Se) powder as Mn and Se precursors respectively at a temperature of 190 °C. The synthesized structures were of flaky morphology with irregular drapes of dimension 5 – 30 nm in width and 100 – 500 nm in length. However, the exact mechanism leading to the formation of these morphological nanostructures was not clearly understood [45].

Solvothermal process was used to synthesize MnSe nanostructures of various shapes, sizes and crystallographic phases by controlling various reaction parameters (Fig. 3). The effects of such parameters in controlling such behavior of the MnSe nanostructures are discussed below.

i) The effect of route adopted for dispersion of the reactants into the solvent

Nanospheres with diameter of $\sim$ 200 nm were synthesized via vigorous pre-stirring of the mixture of Se precursor (Se powder), Mn precursor ($MnCl_2 \cdot 4H_2O$), reducing agent (KBH_4) and the solvent (ethanol amine, EA) used in the solvothermal method. The nanospheres were then converted to nanorods (diameter of 50 – 60 nm and lengths of 1 – 3 μm) and nanowires (diameter 5 – 10 nm) with additional ultrasonic pretreatment of the reaction mixture mentioned above, for 20 min before autoclaving.

The route adopted for dispersion of the reactants into the EA solvent was found to directly influence the shape of the resulting MnSe entities formed. Direct addition of the Mn and Se precursors without stirring or ultrasonication resulted in the formation of α-MnSe nanospheres. Vigorous stirring of the reaction mixture before the start of the solvothermal process was inferred to have accelerated the speed of reaction of the Mn and Se precursors as also the nucleation process, thus resulting in the MnSe microspheres. Partial substitution of the stirring process by ultrasonication of the reaction mixture resulted in MnSe nanorods. It was concluded that the ultrasonication process was promoting the preferential complexation of Mn^{2+} ions with ethanol amine solvent; and the resultant isotropic nature of the reaction mixture led to the formation of MnSe nanorods [46].

ii) The effect of mixtures of various of solvents used

The solvothermal process carried out in a three-neck flask heated at $\sim$ 235 °C for 4 hours under the flow of Ar gas in a Schlenk line resulted in the formation of WZ MnSe nanostructures. The solvent used in this process was a mixture

TABLE 1. Summarized data of MnSe nanostructures synthesized by hydrothermal method*

Year Ref.	**Mn precursor/ Se precursor**	**Crystallographic phase**	**MnSe product**	**Temperature** (°C)	**Average size (nm)**	**Method used for determining the size**
2004, [36]	$Mn(CH_3COO)_2 \cdot 4H_2O$/Se powder	α-MnSe	Nanorod	180	200	Transmission electron microscopy (TEM)
			Nanocube	100	80	TEM
2013, [37]	$MnCl_2 \cdot 4H_2O$/Se powder	α-MnSe	Rod like particles	60	100 (Base diameter), (25 Tip diameter)	TEM
2017, [20, 38]	$MnCl_2 \cdot 4H_2O$/ SeO_2	γ-MnSe	Spherical QDs	180	5 & 14	High resolution transmission electron microscopy (HRTEM)
2019, [39]	$MnCl_2 \cdot 4H_2O$/ SeO_2	α-MnSe	Spherical QDs	180	5 to 11	HRTEM
2016, [40]	$Mn(CH_3COO)_2 \cdot 4H_2O$/ NaHSe	α-MnSe	Nanodisc	180	80 to 1500	TEM
2019, [41]	$MnCl_2 \cdot 4H_2O$/ SeO_2	α-MnSe	Spherical QDs	180	20.3 to 46.5(with pH variation)/5 nm	Dynamic light scattering/TEM
2018, [42]	$Mn(CH_3COO)_2 \cdot 4H_2O$/ Na_2SeO_3	α-MnSe	Nanoparticles	180	20 to 30	High-definition field emission scanning electron microscopy (FESEM)
2020, [43]	$MnCl_2 \cdot 4H_2O/SeO_2$	α-MnSe	Multilayer structure with a small quantity of microplates surrounded by lots of nanoplates	180	—	

*Additional details on the product obtained by using hydrothermal method along with other properties have been discussed in Table 3

of oleic acid (OA, 15 mL), and tetraethylene glycol (TEG, 15 mL). Maintaining the OA:TEG ratio at 50:50 resulted in the formation of pure WZ phase MnSe nanoparticles 25 – 75 nm in size but irregular in shape. However, RS type MnSe nanostructures can also be predominantly formed in addition to a relatively smaller quantity of the WZ type MnSe if other types of solvents were used in the synthesis process [5].

iii) The effect of heating rate

One of the prime objectives of any nanomaterial synthesis process is to be able to achieve control over the size distribution and morphology of the resulting product. The solvothermal synthesis process used to produce MnSe offers control over the morphology of the nanostructures through variation in the heating rates of the reaction mixture. The formation of MnSe nanocrystals can be divided into: i) the nucleation phase and ii) the growth phase. Different heating rates ranging from low (2 °C min^{-1}) to medium (15 °C min^{-1}) to rapid (25 °C min^{-1}) was employed during the study [19]. Heating rate was found to have influenced on the formation of different types of nucleation seeds in all the three cases. At the low heat rate, the nucleation seeds were of ZB type over which the WZ type tetrapod structure proliferated. The thermodynamically controlled condition provided by the low heating rate favored the formation of anisotropic tertrapod (WZ phase) growth along the c-axis leading to the highest aspect ratio (4.5 ± 0.6) amongst the MnSe crystal structures formed by employing all three heat rates. Low heating rates, however, is characterized by lower purity of the resulting

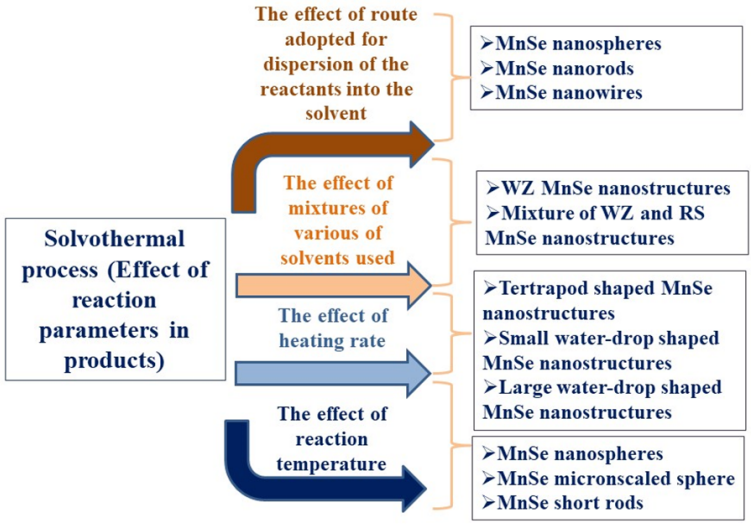

FIG. 3. Diagrammatic representation of effect of reaction parameters on the structure and morphology of the MnSe nanostructures synthesized by solvothermal method

MnSe nanostructures due to presence of both the WZ and ZB structures. Medium heating rates (15 °C min^{-1}) favored the formation of WZ nucleating seeds in addition to minute quantities of ZB phase. The final nanostructure formed consisted of small water-drop shaped MnSe formed by reaction of the MnSe-tetrapod shaped nanocrystals. The water-drop shaped nanocrystals were found to be of uniform size and lower aspect ratios (1.9 ± 0.2) as compared to the product formed via low heating rates (2 °C min^{-1}). Rapid heating rates (25 °C min^{-1}) favored the formation of WZ nucleation over that of the ZB nucleation seeds. The c-axis directional crystal growth was found to be favored for the WZ phase leading to anisotropic growth structures predominantly water-drop shaped but also rod shaped, nanotadpole structures etc. and resulted in the lowest aspect ratios (1.2 ± 0.1) of the MnSe amongst the nanostructures produced via all the three heating rate variations in the solvothermal synthesis [19]. The reaction temperature also plays a vital role on the morphology of the product. The nanospheres which were formed at 180 °C temperature, transformed into micron-scaled spheres and short rods on maintaining the reaction temperature between 100 to 120 °C [46]. Table 2 summarizes the data on synthesis of MnSe nanostructures by solvothermal method.

2.1.3. Hot injection method. The hot injection method is used as the most common synthesis method for obtaining highly monodisperse isotropic nanoparticles with narrow particle-size distribution. This method is based on rapid injection of cold precursor into a mixture of organic solvents heated at high temperatures. Here rapid injection of the precursors facilitates a high degree of supersaturation leading to instantaneous nucleation growth of the nanoparticles from the reaction mixture [47]. Nucleation of the nanostructures leads to homogeneity in diffusion-controlled growth across the reaction mixture thus favoring a size-focusing phenomenon due to delayed growth of larger sized nanoparticles as compared to the smaller ones. With time, Ostwald ripening occurs where smaller sized particles start dissolving in the solution with the simultaneous emergence of larger sized nanoparticles. The emergence of larger sized nanoparticles from the solution on account of Ostwald ripening favors a thermodynamically stable nanostructure due to the higher volume to surface ratio and thus unavailability of greater number of reactive sites on the nanoparticle surface [48]. Thus, the hot injection method separates out the nucleation and growth process efficiently to provide a highly monodisperse size-controlled nanoparticle. The requirement of inert atmospheric and high temperature environment inside the reaction chamber makes the hot injection method challenging for the synthesis of nanoparticles [49–51].

Hot injection method can be used to synthesize α-MnSe nanostructures of different shapes, predominantly cubic and spherical. Using this method, monodisperse α-MnSe nanocubes of morphological purity yield of 100 % were synthesized with average side length of 100 nm. A precise control over the size and morphology of the nanostructures were obtained, resulting in the production of α-MnSe spherical nanoparticles (average size 25 nm as obtained from high resolution transmission electron microscopy (HRTEM)) and α-MnSe nanocubes of uniform side length (50 nm). The variations of the characteristics of the MnSe nanostructures were studied by changing the reaction parameters such as precursor concentration, surfactant composition, the reaction temperature and the reaction time. The formation of aggregated α-MnSe nanocubes at an extended reaction time of 18 hr was concluded as due to the occurrence of "Ostwald Ripening" process [52].

Cubic phase, highly crystalline, monodisperse MnSe nanospheres in the size range of 7 – 16 nm were synthesized by using the hot injection method. Manganese (II) acetate tetrahydrate $(CH_3COO)_2Mn{\cdot}4H_2O$) and Se powder were used as the Mn and Se precursors respectively and oleic acid was used as the capping agent for the production of various sized hydrophobic nanospheres. The size and polydispersity of the nanospheres were controlled by controlling the reaction

TABLE 2. Summarized data on synthesis of MnSe nanostructures by solvothermal method**

Year Ref.	**Mn precursor/ Se precursor**	**Solvent**	**Crystallographic phase**	**MnSe product**	**Temperature (°C)**	**Average size (nm)**	**Method used for determining the size**
2002, [45]	$MnCl_2 \cdot 4H_2O$/Se powder	Ethylene-diamine	α-MnSe	Flaky morphology with irregular drapes	190	5 to 30 (width), 100 to 500 (length)	TEM
2006, [46]	$MnCl_2 \cdot 4H_2O$/Se powder	Ethanol amine	α-MnSe	Nanospheres	180	200 (diameter)	FESEM & TEM
				Nanorods		50 to 60 (diameter), 1 to 3 μm (length)	
				Nanowires		5 to 10 (diameter)	
2010, [5]	Anhydrous $MnCl_2$/Se powder	Mixture of oleic acid & tetraethylene glycol	γ-MnSe	Irregular shaped nanoparticle	235	25 to 75	HRTEM
2012, [19]	Anhydrous $MnCl_2$/Se powder	Mixture of oleic acid & tetraethylene glycol	Mixture of γ-MnSe & β-MnSe	Tetrapod shaped	200–300	148 (arm length), 30 (arm diameter)	TEM
			Mixture of γ-MnSe & β-MnSe	Small water-droplet shape		75 (length), 40 (diameter)	
			γ-MnSe	Large water-droplet shape		265 (length), 210 (diameter)	

**Additional details on the product obtained by using solvothermal method along with other properties have been discussed in Table 3

temperature (200 to 280 °C) of the hot solution of the Mn precursor. Injection of the Se precursor stock solution which was maintained at room temperature ($\sim$ 25 °C) into the Mn precursor solution (200 °C) led to the formation of nanoparticles of average size 7 nm. The size of the nanoparticles increased to 12 and 16 nm (as obtained from high HRTEM) on raising the reaction temperature up to 240 and 280 °C respectively [53]. Fig. 2(c) depicts the schematic diagram of hot injection synthesis process.

2.2. Deposition techniques

Deposition techniques are commonly used synthesis processes for various nanostructures, preferably in the form of thin film that is created and deposited onto a substrate material. Various deposition methods that are used for the synthesis of MnSe nanostructures are chemical vapor deposition, pulsed laser deposition method etc.

2.2.1. Chemical vapor deposition (CVD). Chemical vapor deposition (CVD) is a well-known thin film coating process where thermally induced chemical reactions take place between the precursors/reagents supplied in vapor/gaseous form and the surface of a solid substrate. Highly controlled 2D nanomaterials with high crystal quality, purity and good structural regularity can be synthesized by CVD as compared to the other conventional synthesis procedures [54]. Flow rate, deposition temperature, pressure and reactor geometry are the key parameters that controls the deposition of the film.

Chemical vapor deposition method was used [55] to synthesize one dimensional MnSe nanostructures by using a temperature-controlled regime of reaction site on the Si substrate coated with Au nanoparticles. In this synthesis, $MnCl_2$ and CoSe powders were used as precursors for manganese and selenium respectively. While the temperature range of the precursor's sources were maintained between 1000 – 1100 °C, that of the Si substrate surface-coated with Au nanoparticles on which the actual reaction takes place leading to the formation of various nanostructures, was maintained between 900 – 800 °C. The vapour-liquid-solid phase transition mechanism was inferred to have been followed leading to the formation of the various manganese selenide/silicon-oxide composite nanostructures with the MnSe nanostructures which mostly form one-dimensional crystalline structures. Various morphologies formed were reaction temperature and/or MnSe

and SiO_x growth rate dependent. The gold nanoparticles deposited on the Si substrate catalysed the reaction of the Mn and Se vapor mixture. MnSe was synthesized within the gold nanoparticles which were saturated with the vapor of the individual elements. Similarly, the gold nanoparticles also catalysed the formation of SiO_x from Si vapor and oxygen that diffuses into the nanoparticle along with the Mn and Se vapors. Depending on the temperature/growth rates, different geometries of crystalline MnSe and amorphous SiO_x structures are formed. Apart from MnSe and SiO_x structures, MnO_x domains have also been characterized in some of the nanostructures formed. Various types of MnSe or MnSe/SiO_x nanocomposite structures formed in the CVD technique can be broadly classified into: i) nanowires (MnSe); ii) nanocomposites (MnSe/SiO_x): core-shell nanocables as well as branched nanocables and pea-pod structures; iii) nano-cube/chain network structures (MnSe only). Fig. 4 summarizes various MnSe and MnSe/SiO_x nanocomposite structures formed. Fig. 2(d) depicts the schematic diagram of chemical vapor deposition method.

In another work, polycrystalline manganese selenide thin films of both rocksalt and zinc blende structures were prepared by organometallic chemical vapor deposition (OMCVD) by taking methyl pentacarbonyl manganese (MPCMn) as manganese precursor and diethyl selenium (DES) as selenium precursor. This study shows that MPCMn is not a suitable precursor for OMVPE processes that require high cracking temperatures. MPCMn produces manganese oxide (MnO) at temperature greater than 450 °C [56]. Moreover, the incorporation of elemental carbon or oxygen in the thin film with the use of carbonyl compound was another drawback obtained of the study.

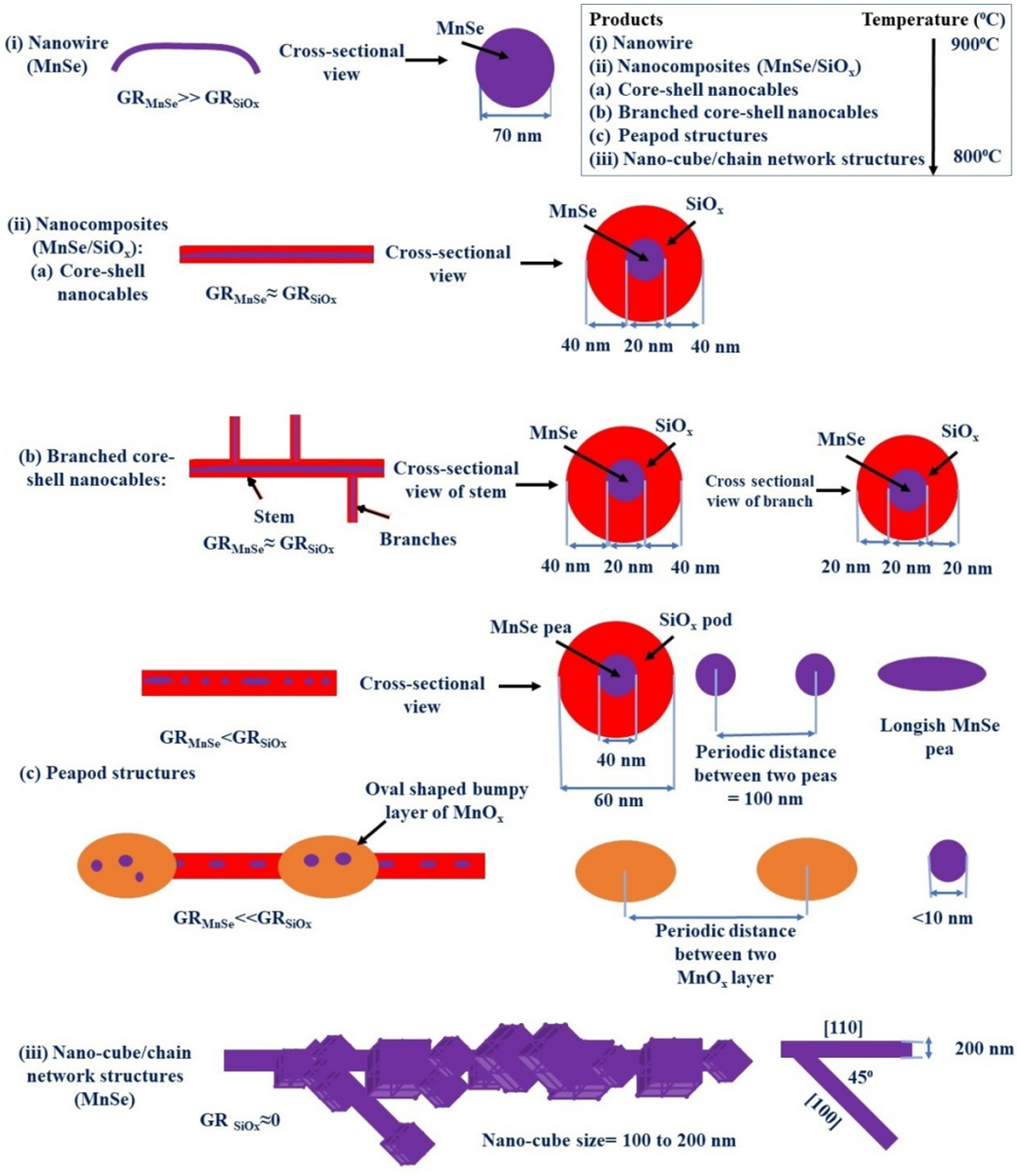

FIG. 4. Schematic diagram (not to scale) of various MnSe nanostructures produced by using CVD method [55]

Ultrathin two-dimensional zinc blende phase manganese selenide (2D β-MnSe) nanosheets were also prepared by the CVD process. The MnSe flakes that were forming the nanosheets were prepared on a mica substrate by using Se powder as the Se precursor and $MnCl_2$ as the Mn precursor and keeping them in a quartz boat (Se) and an alumina boat (Mn) respectively. Both the boats were placed in two different zones of a heating furnace equipped with a quartz tube. Pre-treatment of the quartz tube was done by purging it with Ar gas for 5 min at 300 standard cubic centimetres per minute (sccm). The precursor sources of Mn and Se were heated up to 300 and 680 °C respectively for 20 min in presence of Ar gas (100 sccm) mixed with H_2 gas (10 – 40 sccm) during the growth. After heating the precursors of Mn and Se to the required temperatures (300 and 680 °C) the furnace was kept idle for 10 min to finish the growth of β-MnSe flakes followed by rapid cooling to room temperature. During the growth process, the Ar-H_2 gas mixture helped in controlling precursor vapor transportation and, hence, the morphology and size of MnSe flakes. While the average thickness of the β-MnSe flake can be tailored to 3.5 nm, the lateral size of the flake can be measured in multiples of 12 μm. Stochiometric calculations of the β-MnSe flake revealed the presence of Mn and Se elements in equal proportions. The growth of β-MnSe flakes were reported to be significantly affected by the flow rate of H_2. When the flow rate of H_2 increases from 10 to 35 sccm, the flakes' shapes evolve gradually from simple triangular shape to windmill, dendrite, and eventually more morphologically complex snowflakes shapes with increasing fractal dimensions from 1.02 to 1.4. As inferred, evolution of this β-MnSe flakes from simple to complex structures are dominated by diffusion-controlled kinetics. With lower flow rate of H_2 simple triangular shaped MnSe flakes were formed due to the adequate diffusion of Mn and Se atoms of MnSe in the mica substrate. However, higher flow rate of H_2 leads to increase of the diffusion rate of Mn and Se providing sufficient precursor to create more complicated structure. In addition, during the formation of complex structure in rich H_2 environment, Mn terminated edge growth becomes more energetically favorable [57].

2.2.2. Pulsed laser deposition. A pulsed laser deposition (PLD) method is a physical vapor deposition (PVD) method which is carried out in a vacuum environment to produce multilayer films composed of two or more materials [58, 59]. In this process, with high laser energy density, laser pulses are focused on the targeted pellets which were then vaporized and the resulting ablation plum containing the atoms and the energetic ions of the vaporized material was deposited as a thin film on the substrate material. The high ablation rate of pulsed laser deposition ensures multicomponent thin film formation with desired stoichiometry ratio [60].

By forming pellets of 1.3 cm diameter from a mixture of Mn and Se powder (Mn to Se ratio of 1:1.5), and considering these pellets as ablated targets, PLD was used to form cubic structured MnSe thin films of 200 nm thickness (as determined by using scanning electron microscope (SEM)) in 30 minutes. The laser beam of wavelength 355 nm with laser energy intensity 2 J/cm^2 was created by the third harmonic frequency of a Q-switched Nd:yttrium aluminum garnet (YAG) laser. The laser pulses were used in a repetition rate of 10 Hz and the width was of 10 ns for this process. Moreover, the experiment was carried out by keeping the targeted pellets in a chamber of base pressure of 10^{-2} Pa and 5 Pa during the deposition process. The substrate material used for the deposition of MnSe thin film was stainless steel maintained at a temperature of 200 °C and kept at a distance of 4 cm from the target [61]. Fig. 2(e) depicts the schematic diagram of pulsed laser deposition method.

3. Optical properties of MnSe nanocrystals

UV-visible (UV-Vis) spectroscopy and photoluminescence spectroscopy (PL) are the two main spectroscopic techniques that are used to evaluate the optical properties of nanoparticles.

UV-V is spectroscopy is a technique to study the electronic transition of materials which manifest across the near IR, visible and the UV region of the electromagnetic spectrum. It is a powerful technique to study the interband electronic transition in semiconductors. By using the first absorption peak of absorption spectra of nanoparticles, the band gap (E_g) of the corresponding nanoparticles can be obtained by using the following standard equation:

$$E_g = \frac{1240}{\lambda} \quad (\text{eV}), \tag{1}$$

where λ is the wavelength (in nm) corresponding to the first absorption peak.

Photoluminescence is the emission of light after the absorbing a photon. The physical processes involved in photoluminescence are more complicated than those in absorption because it also involves the emission relaxation mechanism in the material. For direct band gap semiconductor materials, the bottom of the conduction band (conduction band edge, E_c) and the top of the valence band (valence band edge, E_v) occur at the same wave vector k (with $k = 0$) providing change of momentum $\Delta k = 0$. In this case, during photon emission, accompanied by band-to-band transition, an electron recombines with a hole [62].

For indirect band gap semiconductor materials, the bottom of the conduction band does not occur at the momentum $k = 0$, i.e. it is shifted with respect to the top of the valence band. Therefore, any transition process from the bottom of the conduction band to the top of the valence band does not conserve momentum. As the photon is very light particle having no rest mass it cannot carry large momentum. Therefore, a particle such as phonon (quantized lattice vibration) is required that carries the momentum to conserve in the transition process. Thus, in indirect band gap semiconductor for conservation of the momentum in the transition process a phonon must be involved when the photon is emitted [63].

This makes it a second-order process, with a relatively low transition probability. Fig. 5 depicts the schematic diagram of direct and indirect band gap semiconductors.

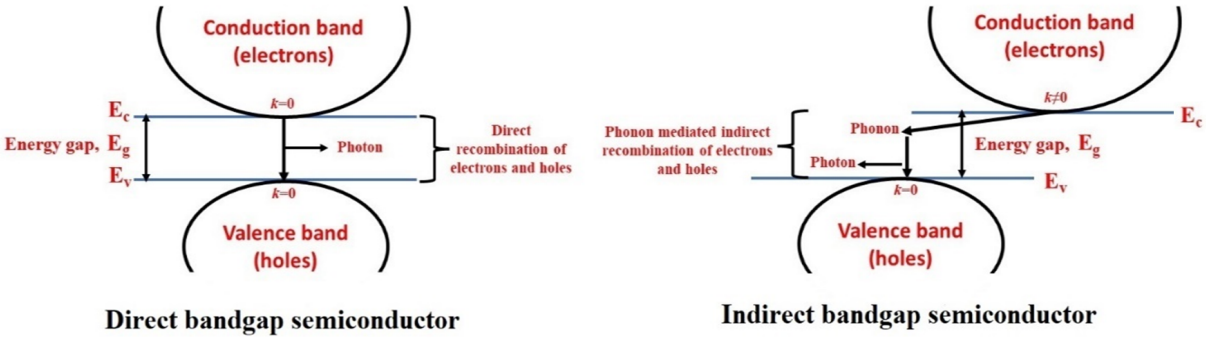

FIG. 5. Schematic diagram of direct and indirect band gap semiconductors

There are various parameters such as size [64], shape, surface capping agents, precursor concentration, reaction time, reaction temperature, the dispersing medium etc. which the optical properties of the nanostructures is relied on [65]. Recent years, one observes focusing of the study on optical properties of MnSe nanostructures caused by increasing area of optical and optoelectronic applications. However, very few reports have been published on the optical properties of MnSe nanostructures.

We discuss below the absorption and photoluminescence (PL) properties of MnSe nanostructures synthesized using different processes.

3.1. UV-Vis response of MnSe nanostructures synthesized by hydrothermal method

Hydrothermally synthesized cubic structured MnSe nanorods were characterized by two absorption peaks at $\sim$ 372 and $\sim$ 437 nm. The peak at 372 nm is blue-shifted from the bulk cubic MnSe (468 nm), signifying strong quantum confinement effects resulting in the MnSe nanorods (372 nm). The corresponding band gap for the MnSe nanorod was found to be 3.33 eV which is blue shifted by an amount of ~ 0.83 eV from the bulk MnSe band gap (E_g) of 2.5 eV [37].

Hydrothermal synthesis method was used to synthesize MnSe nanoparticles having different crystallographic phase and with different UV-Vis spectroscopic behavior by changing the Mn and Se precursor ratio (Mn^{2+}:Se^{2-}). WZ phase MnSe QDs were prepared by keeping the following ratio: Mn^{2+}:Se^{2-}=2:1, which exhibited absorption feature at $\sim$ 303 nm ($E_g = 4.09$ eV) with a blue shifted energy of ($\Delta E \sim 0.59$ eV) from the bulk value of the WZ type MnSe ($E_g = 3.5$ eV). With increasing this precursor concentration ratios up to 3:1 and 4:1, the absorption peak maxima were red shifted to $\lambda = 408$ nm ($E_g = 3.03$ eV) from $\sim$ 303 nm that was observed for 2:1 with an adequate blue shifting of ($\Delta E \sim 0.5$ eV) with respect to the bulk RS type structure ($E_g = 2.5$ eV). It was suggested that incorporation of excess amount of Mn^{2+} concentration in MnSe QDs prepared by taking precursor ratio 3:1 and 4:1 there was a probability of partial phase transformation of the WZ phase to an RS one [20]. By varying the type of capping material like TGA and SDS molecules, WZ MnSe nanoparticles were seen to exhibit significant variation in absorption behavior. The absorption peak which was observed at 303 nm ($E_g = 4.09$ eV) for TGA capped MnSe QDs significantly red shifted to 330 nm ($E_g = 3.75$ eV) while capped by SDS keeping the precursor ratio same. Thus, in hydrothermal method the optical properties of the MnSe nanostructure can be significantly altered by the precursor concentration ratio and the type of capping material used [38]. Fig. 6(i) depicts the change of excitonic wavelength of first excitonic absorption peak of MnSe nanostructures with precursor concentration ratio and type of capping agent used in the hydrothermal method.

3.2. UV-Vis response of MnSe nanostructures synthesized by solvothermal method

Cubic MnSe nanospheres synthesized via solvothermal process exhibited two broad peaks at around 336 nm and 419 nm and a weak shoulder peak centered at about 594 nm [66]. The WZ MnSe nanostructures of various shapes and sizes, synthesized by this method exhibit dependence of absorption spectra behavior with heating rates used in the synthesis process [19]. First absorption peaks at 389 nm ($E_g = 3.2$ eV) and 391 nm ($E_g = 3.17$ eV) were observed for tetrapod shaped (size 30 nm) and small water-drop shaped (size 40 nm) MnSe nanostructures respectively for the heating rates of 2 and 15 °C. Red shifting of the absorption peak to 398 nm from 391 was clearly observed for the larger sized water-drop shaped (size 210 nm) MnSe nanoparticles synthesized by using heating rate of 25 °C. However, in case of all differently shaped nanoparticles the band gaps obtained were found slightly smaller than the bulk WZ type MnSe of 3.5 eV. Fig. 6(ii) shows the change of excitonic wavelength of the first absorption peak of MnSe nanostructures with heating rate used in the solvothermal method.

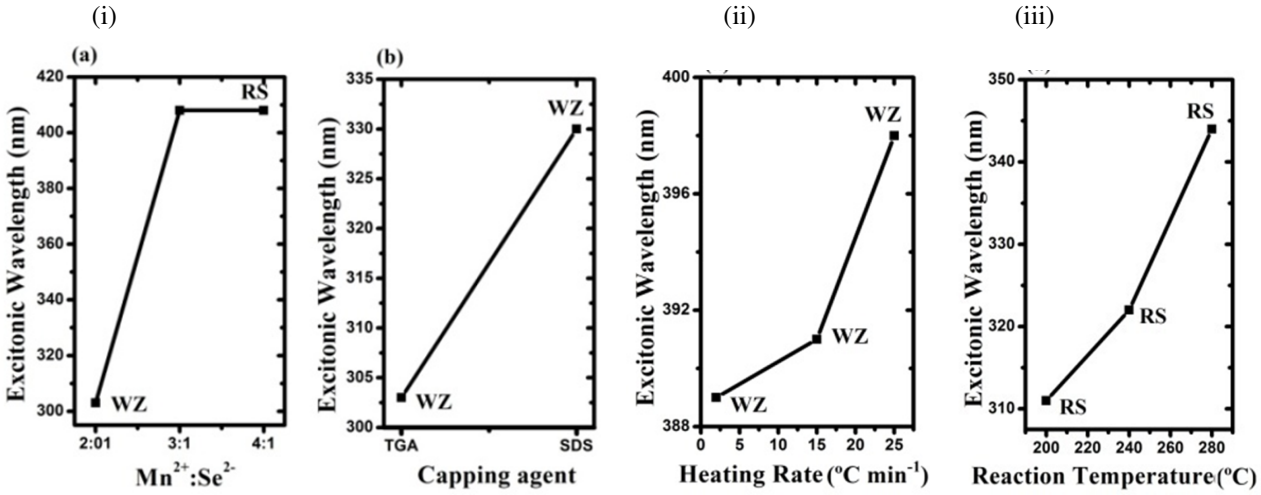

FIG. 6. i) Change of excitonic wavelength of MnSe nanostructures with a) precursor concentration ratio and b) type of coating (capping) agent used in hydrothermal method; ii) Change of excitonic wavelength of MnSe nanostructures with heating rate used in solvothermal method; iii) Change of excitonic wavelength of MnSe nanostructures with reaction temperature used in hot injection method

Size dispersion in the case of water-drop-shaped MnSe nanoparticles was attributed to the exhibition of broadening of the absorption peak width observed in this type of MnSe nanostructure [19]. The wurtzite shaped MnSe nanoparticles produced by solvothermal method was the first reported with a band gap in the range of 3.5 – 3.8 eV [5].

3.3. UV-Vis response of MnSe nanostructures synthesized by hot injection method

Similar to the effect of heating rates on the absorption peaks of nanostructures as synthesized by the solvothermal process, reaction temperature can also influence the quantum confinement of MnSe nanostructures as obtained by the hot injection method. Absorption peaks of cubic MnSe spherical nanoparticles red shifted from 311 to 322 nm and from 322 to 344 nm on increasing the reaction temperature from 200 to 240 °C and from 240 to 280 °C; respectively thus indicating an increase in size of the nanoparticles. The nanoparticles having the largest size (16 nm) blue shifted by an amount of 1.11 eV from cubic bulk MnSe indicating effective quantum confinement of charge carriers [53]. Fig. 6(iii) depicts the change of excitonic wavelength of MnSe nanostructures with reaction temperature used, in hot injection method.

3.4. Comparison of UV-Vis response of MnSe nanostructures synthesized by different method

It can be observed that in both cubic and wurtzite MnSe nanostructures synthesized by different methods, the blue shifting from the corresponding bulk MnSe band gaps are very small. For WZ MnSe nanostructures the highest blue shifted energy was observed to be 0.59 eV from the bulk WZ MnSe band gap (3.5 eV). The corresponding energy is maximum of 1.48 eV for cubic MnSe nanostructures that is shifted from cubic MnSe band gap (2.5 eV). The observed lower value of blue shifted energy may be due to the highly localized nature of 3d electronic bands of Mn atoms in the nanostructures [67]. While comparing the first absorption peak of cubic MnSe nanostructures synthesized by different methods, the position of this peak is observed to be significantly different. For cubic MnSe nanorods synthesized by hydrothermal method this peak was found to be located at 372 nm while, for cubic nanoparticles synthesized by solvothermal and hot injection method the peaks were found to be located at 336 nm and 311 nm respectively. Thus, the blue shifted energy for the cubic MnSe nanostructure synthesized by hot injection method was observed to be the largest ($\Delta E = 1.48$ eV). In case of WZ MnSe nanostructure, the first absorption peak for hydrothermally synthesized QDs was observed to be located at significantly lower wavelength (303 nm) as compared to the nanostructures synthesized by solvothermal method (389 nm). Fig. 7 show the variation of the first excitonic peak position of (a) cubic and (b) WZ MnSe nanostructures with the method of synthesis.

Moreover, the cubic structured MnSe nanorods synthesized by the hydrothermal method exhibited two absorption peaks (372 and 437 nm). One of the peaks was attributed to the electronic transition in the core state and the other one to the electronic transitions in the surface states. Similar to the hydrothermal method, solvothermally synthesized cubic MnSe nanoparticles also exhibited two absorption peaks (336 and 419 nm) and a shoulder peak (594 nm). The shoulder peak is dependent on the type of the solvent used in the nanoparticle synthesis process. However, the cubic structured MnSe nanoparticles synthesized by hot injection method showed only a single absorption peak in the UV Vis spectra. Thus, the absorption behavior can be significantly altered by changing the synthesis procedure used for the MnSe nanostructures in addition to the reaction parameters used in a specific process. Similar behavior has been also observed

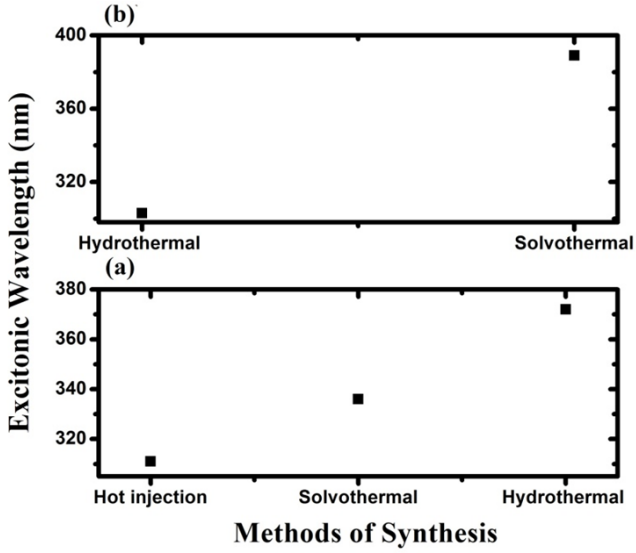

FIG. 7. Variation of the first excitonic peak position of (a) cubic and (b) WZ MnSe nanostructures with the method of synthesis (y-axis-excitonic wavelength, x-axis-methods of synthesis)

for other nanoparticles [68]. Table 3 depicts the summarized data obtained from UV-Vis spectroscopy study of MnSe nanostructures synthesized by various methods.

3.5. PL response of MnSe nanostructures synthesized by hydrothermal method

To get the photoluminescence spectra, the nanostructures were excited by a wavelength lower than the wavelength corresponding to the band gap. For a defect-free nanomaterial, the emission due to the corresponding excitation will lie at the band gap region only and is known as band edge emission. Whereas a nanomaterial having multiple defects (point defects, surface defects etc.) shows emissions in the direct band gap region as well as in other regions at higher wavelengths than the direct emission wavelength. These emissions corresponding to higher wavelength region are known as defect related emissions.

Important characteristics of nanostructures such as the suppression or improvement of the photoluminescence intensity, the ratio of band gap to defect related emission intensity (I_{BE}/I_{DE}), quantum yield (Φ_Q) and stability are dependent on the reaction parameters and the nature of the surfactant capping material on the nanostructures.

Different PL behavior was observed for MnSe QDs prepared with different Mn and Se precursor concentration ratios (Mn^{2+}: Se^{2-}). With increasing precursor ratio (Mn^{2+}: Se^{2-}), red shifting of the emission spectra was observed for the QDs when excited with a constant excitation wavelength, $\lambda_{ex} = 300$ nm. The emission maxima observed at ~ 400 nm for MnSe QDs prepared with Mn^{2+}: Se^{2-}=2:1 was red shifted to ~ 535 nm for the QDs synthesized with higher precursor ratios of 3:1 and 4:1 The corresponding band edge emission (λ_{BE}) peaks were located at 400, 515 and 517 nm. The positions of the defect related emission (λ_{DE}) peaks were 459, 554 and 566 nm.

By varying the type of the surfactant, the behavior of the PL spectra could be tuned significantly. The band edge emission (λ_{BE}) and defect related emission (λ_{DE}) peaks of TGA capped WZ MnSe QDs synthesized by hydrothermal method were found to be located at ~ 368 and 400 nm respectively ($\lambda_{ex} = 300$ nm). However, on changing the capping agent to SDS, the λ_{BE} was shifted to ~ 365 nm and the λ_{DE} to ~ 405 nm. The intensity ratio (I_{BE}/I_{DE}) between band edge emission and defect related emission were found to be nearly ~ 0.4 and ~ 0.78 respectively for TGA and SDS capped MnSe QDs. The defect related emission in MnSe QDs was expected to arise from the defects present in the metastable WZ MnSe nanocrystal core [69].

The red shift of the emission peak with respect to the absorption peak of a nanoparticle is known as Stokes shift, which reveals the energy losses between absorption and emission [70]. This is one of the most important characteristics that influence on the optical properties of nanostructures. Stokes shift is commonly observed in semiconductor QDs and originates from surface states (vacancies and dangling bonds) and interstitial states (interstitial atoms and vacancies) acting as sites for the recombination of electron and hole [71]. Moreover, Stokes shifts of colloidal QDs are related to phonon interactions [72]. The authors of this review article have considered the shifting of the emission peak maxima from the absorption peak maxima of the QDs while calculating the Stokes shift. It was observed that the emission peak maxima at ~ 400 nm ($E_g = 3.1$ eV) for MnSe QDs synthesized with Mn^{2+}/Se^{2-}: 2:1, was significantly shifted by ~ 97 nm ($\Delta E_g = 910$ meV) from the excitonic absorption peak position of ~ 303 nm ($E_g = 4.09$ eV) as per calculations by the authors. The shifting has been calculated to be 127 nm ($\Delta E_g = 730$ meV) for the QDs synthesized with Mn^{2+}/Se^{2-} ratio of 3:1 and 4:1. For different capping agents TGA and SDS the Stokes shifts are calculated to be 84 nm ($\Delta E_g = 890$ meV) and 47 nm ($\Delta E_g = 470$ meV), respectively. MnSe QDs exhibiting extremely large Stokes shifts (in the range of 470

TABLE 3. Summarized data on UV visible spectroscopic properties of MnSe nanostructures

Synthesis Method	**Crystallographic phase**	**Shape**	**Parameter change**		**Size (diameter) (nm)**	**Excitonic Wavelength, λ (nm) of the 1stabsorption peak**	**E_g (eV)**	**Blue shifted energy (eV) from RS bulk ($E_g = 2.5$ eV)/WZ bulk (3.5 eV)**
Hydrothermal [36]	α-MnSe-	Nanorods	—		100	372	3.33	0.83 (from RS)
Hydrothermal [20]	γ-MnSe	Spherical	Change of Mn^{2+}: Se^{2-}	2:01	7	303	4.09	0.59 (from WZ)
	α-MnSe	—		3:1	—	408	3.03	0.5 (from RS)
	α-MnSe	—		4:1	—	408	3.03	0.5 (from RS)
Hydrothermal [37]	γ-MnSe	Spherical	Change of type of capping agent	TGA	5	303	4.09	0.59 (from WZ)
				SDS	14	330	3.75	0.25 (from WZ)
Solvothermal [65]	α-MnSe	Spherical	—	—	200	336	3.69	1.1 (from RS)
Solvothermal [19]	Mixture of γ-MnSe & β-MnSe	Tetrapod shaped	Change of heating rate	2 °C min^{-1}	30	389	3.2	—
	Mixture of γ-MnSe & β-MnSe	Small waterdrop shaped		15 °C min^{-1}	40	391	3.17	—
	γ-MnSe	Large waterdrop shaped		25 °C min^{-1}	210	398	3.11	—
Solvothermal [5]	γ-MnSe	Irregular	—	25–75		350	3.54	0.04 (from WZ)
Hot injection [52]	α-MnSe	Spherical	Change of reaction temperature	200 °C	7	311	3.98	1.48 (from RS)
				240 °C	12	322	3.85	1.35 (from RS)
				280 °C	16	344	3.60	1.1 (from RS)

to 910 meV) are of interests for use as a down-conversion phosphor [73], and in high-quality (high sensitivity and high spatial resolution) bioimaging response [74, 75]. Large Stokes shift in nanomaterials leads to reducing of the probability of the self-absorption mechanism and, hence, the fluorescence quenching that arises from the overlapping of absorption and emission spectra [70, 76].

Typically, the fluorescence quantum yield (Φ_Q) gives the efficiency of any process exhibiting fluorescence phenomenon. It is defined as the ratio of the number of photons emitted to the number of photons absorbed. In general,

$$\Phi_Q = \frac{N_e}{N_a}, \tag{2}$$

where N_e is the number of emitted photons, N_a is the number of absorbed photons.

The quantum yield (Φ_Q) of the QDs can be predicted more accurately using the following relation [77]:

$$\Phi_Q \cdot 100 = Q_{\text{ref}} \left(\frac{n}{n_{\text{ref}}}\right)^2 \frac{I_Q}{I_{\text{ref}}} \frac{A_{\text{ref}}}{A_Q}. \tag{3}$$

The Q_{ref} represents the quantum yield of a reference specimen; I_Q and I_{ref} are the integrated emission intensities of QDs and reference respectively; A_Q and A_{ref} are the absorption intensities of QDs and reference respectively; n (sample) and n_{ref} (reference) are the refractive indices of the solvents of sample and reference respectively. By taking Rhodamine 6G® as the reference, MnSe QDs coated with TGA showed significantly larger values (~ 3 fold) of Φ_Q (75 %) as compared to the SDS coated ones (24 %) [38].

The dynamics of different emission behaviors exhibited by the QDs capped by various functionalizing materials can be studied by time resolved photoluminescence (TRPL) spectroscopy. TRPL can also resolve the spectral and decay kinetic properties of nanostructures [78].

The study of TRPL spectra of TGA and SDS capped MnSe QDs revealed that in the both cases the capped MnSe QDs exhibited bi-exponential decay behavior accompanied by fast (τ_1) and slow (τ_2) decay parameters. The presence of both fast and slow time components in TRPL spectra indicates that two distinct emitting states having different lifetimes are involved in the visible pholuminescence process of the QDs [79]. Parameter τ_1 corresponds to direct exciton recombination emission whereas τ_2 corresponds to surface trapped emission associated with the carriers trapped at the surface sites for the respective nanostructure. The values of τ_1 and τ_2 for MnSe-TGA QDs were found to be ~ 0.65 and ~ 3.05 ns, respectively, and for MnSe-SDSQDs the corresponding values were $\tau_1 \sim 1.04$ ns, and $\tau_2 \sim 5.11$ ns.

The average life time of the QDs were calculated by using the following expression: [80, 81],

$$\tau_{\text{average}} = \frac{A_1\tau_1^2 + A_2\tau_2^2}{A_1\tau_1 + A_2\tau_2^3},$$

where A_1 and A_2 are the pre-exponential factors for the fast and slow processes respectively.

The average life time values were found to be ~ 0.87 and ~ 1.20 ns for MnSe-TGA and MnSe-SDS QDs respectively. Alkyl chains of SDS molecules which were six times longer as compared to TGA molecules were believed to be responsible for surface passivation while offering QD emission for longer time duration as compared to the TGA counterpart [38, 82–84].

Cubic structured MnSe QDs synthesized by the hydrothermal method, exhibited emission response with the emission peak at $\sim$ 430 nm ($\lambda_{ex} = 300$ nm). When capped with different surfactants such as CTAB, TGA and dextran, the emission peaks were slightly blue shifted to 428 nm. In the both cases (coated and uncoated QDs), the emission response was very symmetric with FWHM (full width at half maximum) of 11 nm [39]. Lower FWHM of the QDs signifies higher probability of uniform emission energies and uniform physical properties such as size, strain and composition etc. throughout the sample [85]. The relaxation time study of the uncoated and surfactant coated QDs showed significant variation of the relaxation time (τ_2) related to surface trapped emissions but almost a constant value of relaxation time (τ_1) related to band edge emission. The maximum τ_2 was observed for dextran coated MnSe QDs ($\tau_2 = 5.5$ ns), whereas on capping by TGA the QDs exhibited significantly lower τ_2 ($\tau_2 = 2.7$ ns) as compared to the dextran capped one (by a factor of 2.03). Hence, capping of QDs using surfactants such as short chain type (TGA) and long chain polysaccharide types dextran leads to different types of surface behaviour of the QDs (different values of $\tau 2$) [38, 39, 86]. Larger hydrophilic cross-sectional area formed by the dextran molecules around the QDs, helps in filling vacancies and surface defects enhancing surface passivation.

3.6. PL response of MnSe nanostructures synthesized by solvothermal method

Similar to the hydrothermally synthesized MnSe QDs, α-MnSe nanospheres synthesized by solvothermal method exhibited two emission peaks due to near band edge and defect related emissions ($\lambda_{ex} = 365$ nm). The intensity of the defect related emission peak observed at $\sim$ 437 nm is comparatively higher (by factor of 1.1) than that of the band edge emission peak located at $\sim$ 416 nm [87]. If we calculate the corresponding Stokes shift for these α-MnSe nanospheres it is observed that the emission peak maxima positioned at $\sim$ 416 nm ($E_g = 2.98$ eV) is significantly shifted by 710 meV ($\sim$ 80 nm) from the excitonic absorption peak position at $\sim$ 336 nm ($E_g = 3.69$ eV).

MnSe nanoparticles of wurtzite phase (γ-MnSe) having different shapes exhibit smaller Stokes shift as compared to that of cubic phase (α-MnSe) nanospheres. These nanostructures having tetrapod shapes show a Stokes shift of 11 nm from the absorption maxima at 389 nm to the emission maxima at 400 nm. Similar amount of Stokes shift (11 nm) is observed for small water-droplet nanospheres (absorption maxima 391 nm, emission maxima 402 nm). However, for the large water-droplet shaped nanostructures, the Stokes shift steeply decreases to 7 nm (absorption maxima 398 nm, emission maxima 405 nm) [19]. Thus, different shapes and hence different aspect ratios (length/diameter) have a direct influence on the Stokes shift for nanostructures. The Stokes shift of the anisotropic nanostructures does not change while the aspect ratio changes from 4.5 ± 0.6 (tetrapod shaped) to 1.9 ± 0.2 (small water-droplet shaped). But surprisingly with a sudden decrease of the aspect ratio from 1.9 ± 0.2 (small water-droplet shaped) to 1.2 ± 0.1 (large water-droplet shaped), the Stokes shift reduces to 7 nm. Therefore, it can be observed that the nanostructures with less aspect ratio showed lower Stokes shift as compared to that of nanostructures with higher aspect ratio. Different aspect ratios of the MnSe nanostructures resulted in energy fluctuations and thus providing variations in the calculated Stokes shift. The dependence of Stokes shift on the aspect ratio as observed for MnSe nanostructures were also reported for other nanostructures including CdSe/ZnS Core/Shell Nanorods [88, 89]. This type of size dependent Stokes shift has been

observed for other nanoparticles including CdSe Quantum dots [19, 90, 91]. Fig. 8(a) depicts the variation of Stokes shift with aspect ratio of cubic phase MnSe nanostructures synthesized by solvothermal method.

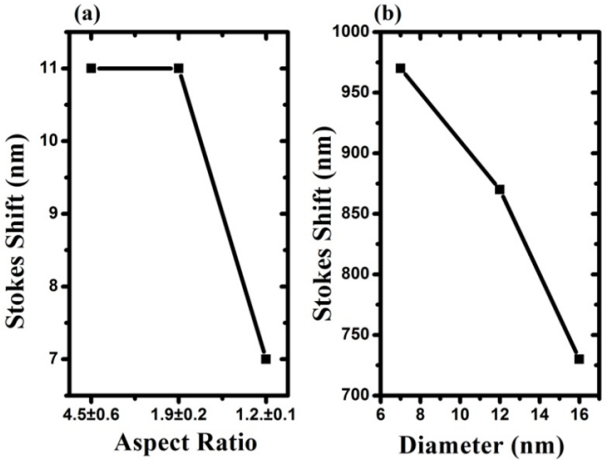

FIG. 8. Variation of Stokes shift with (a) aspect ratio of α-MnSe nanostructures synthesized by solvothermal method and (b) diameter of γ-MnSe nanostructures synthesized by hot injection method

3.7. PL response of MnSe nanostructures synthesized by hot injection method

Two emission peaks corresponding to band edge emission and defect related emission can be observed in MnSe nanostructures synthesized by hot injection method. The both peaks are significantly red shifted with an increase in size (diameter) of the nanoparticles. The position of band edge emission peak (λ_{BE}) was observed to have shift from 407 to 418 nm with the increase in size of the nanoparticles from 7 to 12 nm. The λ_{BE} for 16 nm sized nanoparticle was found to be located at 427 nm. The defect related emission peaks are positioned at 442, 474 and 495 nm for 7, 12 and 16 nm MnSe nanoparticles, respectively. Variation of emission peaks with the size of nanoparticles signifies effective quantum confinement behavior. The change of emission response with size in MnSe nanoparticles makes it a promising material that can be used in light emitting devices in the ultraviolet region. Similar size dependent PL emission response was observed for MnS nanocube structures and other various nanostructures including CdSe QDs [92]. The intensity of defect related emission peaks showed a dominant response over the intensity of band edge related emission peaks with increase in size of the nanoparticles. It was concluded that surface passivation in nanoparticles of different sizes could influence on the intensity of band edge and defect related emission peaks.

Cubic phase MnSe nanoparticles synthesized by hot injection method exhibited size-dependent Stokes shift values of 970 and 730 meV for nanoparticles of sizes 7 and 16 nm, respectively. Fig. 8(b) depicts the variation of Stokes shift with diameter of WZ MnSe nanoparticles synthesized by hot injection method.

3.8. PL response of MnSe nanostructures synthesized by CVD method

MnSe nanowires synthesized by chemical vapor deposition method exhibited temperature dependent PL spectra with two broad emissions peaks around 413 and 435 nm ($\lambda_{ex} = 325$ nm) and were assumed to be from the band edge emission spectra. It was observed that below -173 °C the nanowires show another emission peak at 751 nm originating from spin forbidden transition. The appearance of this peak signifies the presence of octahedrally coordinated Mn^{2+} sites of the α-MnSe nanostructures. It is observed that the intensities of the band edge emission peaks significantly decrease with the increase in temperature from -266 to 27 °C. TRPL spectra of the nanostructures revealed single exponential decay behavior with average decay time of $\tau_{av} = 18$ μs for the Mn^{2+} transition. The average decay time values were found to remain constant as the temperature was increased from -266 to -173 °C [93].

3.9. Comparison of PL response of MnSe nanostructures synthesized by different methods

The PL spectrum of the MnSe nanostructures prepared using various synthesis techniques, comprised of mainly two emission peaks: band edge and defect related emission. Moreover, the Stokes shift calculated for MnSe nanostructures is very large in magnitude and is dependent on size, crystalline phase and the method of synthesis of the nanostructures. The Stokes shift obtained for MnSe nanostructures was compared for nanostructures synthesized by various synthesis procedures. Cubic phase MnSe nanoparticles exhibited the largest Stokes shift of 970 meV (101 nm) when synthesized by the hot injection method. On the other hand, MnSe nanoparticles of the same crystalline phase exhibited the lowest Stokes shift of 710 meV (80 nm) when synthesized using solvothermal method. Wurtzite phase MnSe nanoparticles exhibited the largest Stokes shift of 910 meV (97 nm) when synthesised by the hydrothermal method. On the other hand, MnSe nanoparticles of the same crystalline phase exhibited the lowest Stokes shift of 50 meV (7 nm) when synthesized

using solvothermal method. Table 4 depicts the calculated Stokes shift values of various MnSe nanostructures prepared by different synthesis procedures.

TABLE 4. Stokes shift calculated for MnSe nanostructures synthesized by various methods

Synthesis method	**Crystalline phase of MnSe**	**Shape**	**Parameter changed**		**Size (diameter) in nm**	**Excitonic wavelength λ in nm (E_g in eV)**	**Emission maxima wavelength λ in nm (E_g in eV)**	**Stokes shift nm (ΔE_g in meV)**
Hydrothermal [20]	γ-MnSe	Spherical	Change of Mn^{2+}: Se^{2-}	2:01	7	303(4.09)	400 (3.1)	97 (910)
	α-MnSe	—		3:1	—	408 (3.03)	535 (2.31)	127 (730)
	α-MnSe	—		4:1	—	408 (3.03)	535 (2.31)	127 (730)
Hydrothermal [38]	γ-MnSe	Spherical	Type of capping agent	TGA	5	303 (4.09)	387 (3.2)	84 (890)
				SDS	14	330 (3.75)	377 (3.28)	47 (470)
Solvothermal [19]	Mixture of γ-MnSe & β-MnSe	Tetrapod shape	Change of heating rate	2 °C min^{-1}	30	389 (3.2)	400 (3.1)	11 (100)
	Mixture of γ-MnSe & β-MnSe	Small water-droplet shape		15 °C min^{-1}	40	391 (3.17)	402 (3.08)	11 (90)
	γ-MnSe	Large water-droplet shape		25 °C min^{-1}	210	398 (3.11)	405 (3.06)	7 (50)
	α-MnSe	Spherical	—		200	336 (3.69)	416 (2.98)	80 (710)
Hot injection [52]	α-MnSe	Spherical	Change of reaction temperature	200 °C	7	311 (3.98)	411 (3.01)	101 (970)
				240 °C	12	324 (3.82)	419 (2.95)	95 (870)
				280 °C	16	344 (3.60)	432 (2.87)	88 (730)

4. Conclusion

We presented a review of various wet-chemical and deposition methods that are used to synthesize α-, β- and γ-MnSe nanostructures. Various reaction parameters influencing on the controlled growth as well the growth mechanism of the MnSe nanostructures is also discussed. The optical properties of the MnSe nanostructures were observed to be dependent on the method of synthesis procedure. UV-Vis spectroscopy studies showed that the blue shifting of absorption peaks of the MnSe nanostructures from the corresponding bulk MnSe band gaps were very small. However, the absorption peak maxima positions as well as the number of absorption peaks were dependent on the synthesis procedure used. Moreover, Stokes shift calculated from the absorption peak and emission peak maxima for the MnSe nanostructures are very large. A very high signal to noise ratio can be achieved when a nanostructure or any fluorescent dye exhibiting Stokes shift typically greater than 80 nm are used in biological imaging applications [94–97]. Time resolved photoluminescence spectroscopy (TRPL) indicates that the MnSe nanostructures synthesized by wet chemical methods exhibit bi-exponential decay characteristics with fast (τ_1) and slow (τ_2) relaxation time components. The both parameters depend significantly on the type of the capping material used in the MnSe nanostructure. Whereas nanostructures synthesized by using chemical vapor deposition exhibit single exponential decay in TRPL. This review article is expected to act as a reference to researchers in the controlled synthesis of MnSe nanostructures that exhibit special optical properties. Keeping in mind unlimited potential of nanostructure advantages, future research on MnSe looks promising in electrical and magnetic applications, biological labeling and in drug delivery applications.

References

[1] Furdyna J.K. Diluted magnetic semiconductors. *J. of Applied Physics*, 1988, **64** (4), R29–R64.

[2] Furdyna J.K. Diluted magnetic semiconductors: An interface of semiconductor physics and magnetism. *J. of Applied Physics*, 1982, **53** (11), P. 7637–7643.

[3] Dietl T. Diluted magnetic semiconductors. In *Handbook on semiconductors*, T.S. Moss ed., 1994, **3b**, Elsevier, Amsterdam Publishing, P. 1254–1329.

[4] Alsaad A. Structural and magnetic properties of Mn-based diluted magnetic semiconductors and alloys. *Physics Research International*, 2009, **2009**, P. 1–4.

[5] Sines I.T., et al. Colloidal synthesis of non equilibrium wurtzite type MnSe. *Angewandte Chemie International Edition*, 2010, **49** (27), P. 4638–4640.

[6] Wu M., et al. Hydrothermal preparation of α-MnSe and $MnSe_2$ nanorods. *J. of Crystal Growth*, 2004, **262** (1–4), P. 567–571.

[7] Bououdina M., Song Y., Azzaza S. Nano-structured diluted magnetic Semiconductors. In *Reference module in materials science and materials engineering*, 2016, Elsevier, Amsterdam Publishing, P. 1–7.

[8] Kacman P. Spin interactions in diluted magnetic semiconductors and magnetic semiconductor structures. *Semiconductor Science and Technology*, 2001, **16** (4), R25–R39.

[9] Wang C., Yang F., Gao Y. The highly-efficient light-emitting diodes based on transition metal dichalcogenides: from architecture to performance. *Nanoscale Advances*, 2020, **2** (10), P. 4323–4340.

[10] Rai D.P., et al. Spin-induced transition metal (TM) doped SnO2 a dilute magnetic semiconductor (DMS): A first principles study. *J. of Physics and Chemistry of Solids*, 2018, **120**, P. 104–108.

[11] Brozek C.K., et al. Soluble supercapacitors: large and reversible charge storage in colloidal Iron-doped ZnO nanocrystals. *Nano Letters*, 2018, **18** (5), P. 3297–3302.

[12] Balti I., et al. Nanocrystals of Zn(Fe)O-based diluted magnetic semi-conductor as potential luminescent and magnetic bimodal bioimaging probes. *RSC Advances*, 2014, **4** (102), P. 58145–58150.

[13] Decker D.L., Wild R. Optical properties of a-MnSe. *Physical Review B*, 1971,**4** (10), 3425.

[14] Bouroushian M. *Electrochemistry of metal chalcogenides*, 2010, Springer, Berlin, Heidelberg Publishing, 358 pp.

[15] Murray R.M., Forbes B.C., Heyding R.D. The preparation and paramagnetic susceptibility of β-MnSe. *Canadian J. of Chemistry*, 1972, **50** (24), P. 4059–4061.

[16] Schlesinger M. The Mn–Se (manganese-selenium) system. *J. of phase equilibria*, 1998, **19** (6), P. 588–590.

[17] Prasad M., et al. Electrical transport properties of manganese selenide. *Materials Chemistry and Physics*, 1991, **30** (1), P. 13–17.

[18] O'Hara D.J., et al. Room temperature intrinsic ferromagnetism in epitaxial manganese selenide films in the monolayer limit. *Nano Letters*, 2018, **18** (5), P. 3125–3131.

[19] Yang X., et al. Morphology-controlled synthesis of anisotropic wurtzite MnSe nanocrystals: optical and magnetic properties. *Cryst. Eng. Comm.*, 2012, **14** (20), P. 6916–6920.

[20] Sarma R., et al. Physical and biophysical assessment of highly fluorescent, magnetic quantum dots of a wurtzite-phase manganese selenide system. *Nanotechnology*, 2014, **25** (27), 275101.

[21] Song G., et al. Core-Shell MnSe@Bi_2Se_3 fabricated via a cation exchange method as novel nanotheranostics for multimodal imaging and synergistic thermoradiotherapy. *Advanced Materials*, 2015, **27** (40), P. 6110–6117.

[22] Chen S.-H., et al. Ultrasmall MnSe nanoparticles as t1-mri contrast agents for in vivo tumor imaging. *ACS Applied Materials & Interfaces*, 2022, **14** (9), P. 11167–11176.

[23] Bharathi M V., et al. Green synthesis of highly luminescent biotin-conjugated CdSe quantum dots for bioimaging applications. *New J. of Chemistry*, 2020, **44** (39), P. 16891–16899.

[24] Chakraborty S., et al. Multifunctional, high luminescent, biocompatible cdte quantum dot fluorophores for bioimaging applications. *International J. of Nanoscience*, 2011, **10**(04n05), P. 1191–1195.

[25] Wang Z., et al. L-Aspartic acid capped CdS quantum dots as a high performance fluorescence assay for Silver ions (I) detection. *Nanomaterials*, 2019, **9** (8), 1165.

[26] Kim J., et al. High-quantum yield alloy-typed core/shell CdSeZnS/ZnS quantum dots for bio-applications. *J. of Nanobiotechnology*, 2022, **20** (1), P.1–12.

[27] Ji X., et al. Fluorescent quantum dots: Synthesis, biomedical optical imaging, and biosafety assessment. *Colloids and Surfaces B: Biointerfaces*, 2014, **124**, P. 132–139.

[28] Chan W.C.W., et al. Luminescent quantum dots for multiplexed biological detection and imaging. *Current Opinion in Biotechnology*, 2002, **13** (1), P. 40–46.

[29] Xing Y., Rao J. Quantum dot bioconjugates for in vitro diagnostics & in vivo imaging. *Cancer biomarkers: section A of Disease markers*, 2008, **4** (6), P. 307–319.

[30] Derfus A.M., Chan W.C.W., Bhatia S.N. Probing the cytotoxicity of semiconductor quantum dots. *Nano letters*, 2003, **4** (1), P. 11–18.

[31] Pradhan N., et al. Efficient, stable, small, and water-soluble doped ZnSe nanocrystal emitters as non-cadmium biomedical labels. *Nano letters*, 2007,**7** (2), P. 312–317.

[32] Pradhan N., et al. An alternative of CdSe nanocrystal emitters: pure and tunable impurity emissions in ZnSe nanocrystals. *J. of the American Chemical Society*, 2005, **127** (50), P. 17586–17587.

[33] Wang C., et al. Aqueous synthesis of mercaptopropionic acid capped Mn^{2+}-doped ZnSe quantum dots. *J. of Materials Chemistry*, 2009, **19** (38), P. 7016–7022.

[34] Zhu D., et al. Green synthesis and potential application of low-toxic Mn: ZnSe/ZnS core/shell luminescent nanocrystals. *Chem. Commun*., 2010, **46** (29), P. 5226–5228.

[35] Pearson R. Hard and soft acids and bases. *J. of the American Chemical Society*, 1963, **85** (22), P. 3533–3539.

[36] Wu M., et al. Hydrothermal preparation of α-MnSe and $MnSe_2$ nanorods. *J. of crystal growth*, 2004, **262** (1–4), P. 567–571.

[37] Moloto N., et al. Synthesis and characterization of MnS and MnSe nanoparticles: Morphology, optical and magnetic properties. *Optical Materials*, 2013, **36** (1), P. 31–35.

[38] Sarma R., Mohanta D. Anomalous carrier life-time relaxation mediated by head group interaction in surface anchored MnSe quantum dots conjugated with albumin proteins. *Materials Chemistry and Physics*, 2017, **187**, P. 46–53.

[39] Deka A., Saha A., Mohanta D. Consequence of surfactant coating on the Raman active modes and highly symmetric blue-emission decay dynamics of cubic phase MnSe quantum dots. *Physica E: Low-dimensional Systems and Nanostructures*, 2019, **113**, P. 226–232.

[40] Sun J., et al. Controlled synthesis of ferromagnetic MnSex particles. *Chinese Physics B*, 2016, **25** (10), P. 107405.
[41] Deka A., Mohanta D. Noticeable size dispersity and optical stability of sodium dodecyl sulphate (SDS)-coated MnSe quantum dots in extreme natural environment. *Applied Physics A*, 2019, **125** (9), P. 1–10.
[42] Sahoo S., et al. Hydrothermally prepared α-MnSe nanoparticles as a new pseudocapacitive electrode material for supercapacitor. *Electrochimica Acta*, 2018, **268**, P. 403–410.
[43] Tang H., et al. Hydrothermally synthesized MnSe as high cycle stability anode material for lithium-ion battery. *Ionics*, 2020, **26** (1), P. 43–49.
[44] Kharisov B.I., Kharissova O.V., ed., *Handbook of greener synthesis of nanomaterials and compounds: volume 1: fundamental principles and methods*. 2021, Elsevier Publishing, 976 pp.
[45] Qin T., et al. α-MnSe crystallites through solvothermal reaction in ethylenediamine. *Inorganic Chemistry Communications*, 2002, **5** (5), P. 369–371.
[46] Lei S., Tang K., Zheng H. Solvothermal synthesis of α-MnSe uniform nanospheres and nanorods. *Materials Letters*, 2006, **60** (13), P. 1625–1628.
[47] Luo Q. Nanoparticles inks. In *Solution processed metal oxide thin films for electronic applications*, Z. Cui, G. Korotcenkov, eds., 2020, Elsevier, New York Publishing, P. 63–82.
[48] Thanh N.T., Maclean N., Mahiddine S. Mechanisms of nucleation and growth of nanoparticles in solution. *Chemical reviews*, 2014, **114** (15), P. 7610–7630.
[49] Donegá de M., Liljeroth C.P., Vanmaekelbergh D. Physicochemical evaluation of the hot-injection method, a synthesis route for monodisperse nanocrystals. *Small*, 2005, **1** (12), P. 1152–1162.
[50] Salaheldin A.M., et al. Automated synthesis of quantum dot nanocrystals by hot injection: mixing induced self-focusing. *Chemical Engineering J.*, 2017, **320**, P. 232–243.
[51] LaMer V.K., Dinegar R.H. Theory, production and mechanism of formation of monodispersed hydrosols. *J. of The American Chemical Society*, 1950, **72** (11), P. 4847–4854.
[52] Li N., et al. Synthesis of high-quality α-mnse nanostructures with superior lithium storage properties. *Inorganic Chemistry*, 2016, **55** (6), P. 2765–2770.
[53] Das K., et al. Size-dependent magnetic properties of cubic-phase MnSe nanospheres emitting blue-violet fluorescence. *Materials Research Express*, 2018, **5** (5), 056106.
[54] Martin P.M. Chemical vapor deposition. In *Handbook of deposition technologies for films and coatings: science, applications and technology*, 2009, William Andrew Publishing, P. 314–361.
[55] Chun H., et al. Morphology-tuned growth of α-mnse one-dimensional nanostructures. *J. of Physical Chemistry C*, 2006, **111** (2), P. 519–525.
[56] Tomasini P., et al. Methylpentacarbonylmanganese as organometallic precursor for the epitaxial growth of manganese selenide heterostructures. *J. of crystal growth*, 1998, **193** (4), P. 572–576.
[57] Zou J., et al. Controlled growth of ultrathin ferromagnetic β-MnSe semiconductor. *Smart Mat.*, 2022, **3** (3), P. 482–490.
[58] Balakrishnan G., et al. Growth of nanolaminate structure of tetragonal zirconia by pulsed laser deposition. *Nanoscale research letters*, 2013, **8** (1), P. 1–7.
[59] Norton D.P. Pulsed laser deposition of complex materials: progress toward applications in pulsed laser deposition of thin films: applications-led growth of functional materials, R. Eason, ed., 2007, Wiley Publishing, P. 1–31.
[60] Zhu X.N., et al. Piezoelectric and dielectric properties of multilayered $BaTiO_3$/(Ba,Ca)TiO_3/$CaTiO_3$ thin films. *ACS Applied Materials & Interfaces*, 2016, **8** (34), P. 22309–22315.
[61] Xue M.-Z., Fu Z.-W. Manganese selenide thin films as anode material for lithium-ion batteries. *Solid State Ionics*, 2007, **178** (3), P. 273–279.
[62] Perkowitz S. *Optical characterization of semiconductors: infrared, Raman, and photoluminescence spectroscopy*, 1993, Elsevier Publishing, 220 pp.
[63] Stepniak G., Schüppert M., Bunge C.-A. Polymer-optical fibres for data transmission. In *Polymer optical fibres*, C.-A. Bunge, T. Gries, M. Beckers, eds., 2017, Woodhead Publishing, P. 217–310.
[64] Alivisatos A.P. Semiconductor clusters, nanocrystals, and quantum dots. *Science*, 1996, **271** (5251), P. 933–937.
[65] Nair A.K., et al. Optical characterization of nanomaterials. In *Characterization of nanomaterials*, S.M. Bhagyaraj, et al. eds., 2018, Woodhead Publishing, P. 269–299.
[66] Lei S., Tang K., Zheng H., Solvothermal synthesis of α-MnSe uniform nanospheres and nanorods. *Materials Letters*, 2006, **60** (13–14), P. 1625–1628.
[67] Heulings, et al. Mn-substituted inorganic?organic hybrid materials based on ZnSe: nanostructures that may lead to magnetic semiconductors with a strong quantum confinement effect. *Nano Letters*, 2001, **1** (10), P. 521–525.
[68] Dwandaru W.S.B., Bilqis S.M., Wisnuwijaya R.I. Optical properties comparison of carbon nanodots synthesized from commercial granulated sugar using hydrothermal method and microwave. *Materials Research Express*, 2019, **6** (10), 105041.
[69] Zhu K., et al. Manganese-doped MnSe/CdSe core/shell nanocrystals: Preparation, characterization, and study of growth mechanism. *J. of Materials Research*, 2011, **26** (18), P. 2400–2406.
[70] Zhou R., et al. Nanocrystals for large Stokes shift-based optosensing. *Chinese Chemical Letters*, 2019, **30** (10), P. 1843–1848.
[71] Bera D., et al. Quantum dots and their multimodal applications: a review. *Materials*, 2010, **3** (4), P. 2260–2345.
[72] Kim S.H., et al. Influence of size and shape anisotropy on optical properties of CdSe quantum dots. *Nanomaterials*, 2020, **10** (8), 1589.
[73] Kundu J., et al. Giant nanocrystal quantum dots: stable down-conversion phosphors that exploit a large stokes shift and efficient shell-to-core energy relaxation. *Nano Letters*, 2012, **12** (6), P. 3031–3037.
[74] Galiyeva P., et al. Mn-doped quinary Ag–In–Ga–Zn–S quantum dots for dual-modal imaging. *ACS omega*, 2021, **6** (48), P. 33100–33110.
[75] Zhou R., et al. Enriching Mn-doped znse quantum dots onto mesoporous silica nanoparticles for enhanced fluorescence/magnetic resonance imaging dual-modal bio-imaging. *ACS Applied Materials & Interfaces*, 2018, **10** (40), P. 34060–34067.
[76] Ren T.-B., et al. A general method to increase stokes shift by introducing alternating vibronic structures. *J. of the American Chemical Society*, 2018, **140** (24), P. 7716–7722.
[77] Deng Z., et al. Water-based route to ligand-selective synthesis of ZnSe and Cd-doped ZnSe quantum dots with tunable ultraviolet a to blue photoluminescence. *Langmuir*, 2009, **25** (1), P. 434–442.
[78] Artesani A., et al. A photoluminescence study of the changes induced in the zinc white pigment by formation of zinc complexes. *Materials*, 2017, **10** (4), 340.
[79] Hung C.-C., et al. Strong green photoluminescence from $In_xGa_{1-x}N$/GaN nanorod arrays. *Optics express*, 2009, **17**, P. 17227–17233.
[80] Sheats G.F., Forster L.S. Fluorescence lifetimes in hydrated bovine serum albumin powders. *Biochemical and Biophysical Research Communications*, 1983, **114** (3), P. 901–906.
[81] Schlegel G., et al. Fluorescence decay time of single semiconductor nanocrystals. *Physical Review Letters*, 2002, **88** (13), 137401.

[82] Telgmann T., Kaatze U. Monomer exchange and concentration fluctuations of micelles broad-band ultrasonic spectrometry of the system triethylene glycol monohexyl ether/water. *The J. of Physical Chemistry A*, 2000, **104** (6), P. 1085–1094.
[83] Yang W., et al. Surface passivation extends single and biexciton lifetimes of InP quantum dots. *Chemical science*, 2020, **11** (22), P. 5779–5789.
[84] Chatterjee A., Maity B., Seth D. Photophysics of 7-(diethylamino)coumarin-3-carboxylic acid in cationic micelles: effect of chain length and head group of the surfactants and urea. *RSC Adv.*, 2014. **4** (64), P. 34026–34036.
[85] Saha J., et al. Enhancing the performance of heterogeneously coupled InAs Stranski-Krastanov on submonolayer quantum dot heterostructures. *Superlattices and Microstructures*, 2019, **135**, 106260.
[86] Bautista M., et al. Surface characterisation of dextran-coated iron oxide nanoparticles prepared by laser pyrolysis and coprecipitation. *J. of Magnetism and Magnetic Materials*, 2005, **293**, P. 20–27.
[87] Lei S., Tang K., Zheng H. Solvothermal synthesis of α-MnSe uniform nanospheres and nanorods. *Materials Letters*, 2006, **60** (13–14), P. 1625–1628.
[88] Li L.-S., et al. Semiconductor nanorod liquid crystals. *Nano Letters*, 2002, **2** (6), P. 557–560.
[89] Mokari T., Banin U. Synthesis and properties of CdSe/ZnS core/shell nanorods. *Chemistry of Materials*, 2003, **15** (20), P. 3955–3960.
[90] Brennan M.C., et al. Origin of the size-dependent stokes shift in $CsPbBr_3$ perovskite nanocrystals. *J. of the American Chemical Society*, 2017, **139** (35), P. 12201–12208.
[91] Placencia D., et al. Synthesis and optical properties of PbSe nanorods with controlled diameter and length. *The J. of Physical Chemistry Letters*, 2015, **6** (17), P. 3360–3364.
[92] Qu L., Peng X. Control of photoluminescence properties of cdse nanocrystals in growth. *J. of the American Chemical Society*, 2002, **124** (9), P. 2049–2055.
[93] Chun H.J., et al. Morphology-tuned growth of α-MnSe one-dimensional nanostructures. *The J. of Physical Chemistry C*, 2007, **111** (2), P. 519–525.
[94] Gao, Z., Hao Y., Zheng M.-L. A fluorescent dye with large Stokes shift and high stability: synthesis and application to live cell imaging. *RSC Adv.*, 2017, **7**, P. 7604–7609.
[95] He X., et al. Fluorescence resonance energy transfer mediated large stokes shifting near-infrared fluorescent silica nanoparticles for in vivo small-animal imaging. *Analytical Chemistry*, 2012, **84** (21), P. 9056–9064.
[96] Zhang S., et al. One-step synthesis of yellow-emissive carbon dots with a large Stokes shift and their application in fluorimetric imaging of intracellular pH. *Spectrochimica Acta Part A: Molecular and Biomolecular Spectroscopy*, 2020, **227**, 117677.
[97] Zhang J., et al. Highly stable near-infrared fluorescent organic nanoparticles with a large stokes shift for noninvasive long-term cellular imaging. *ACS Applied Materials & Interfaces*, 2015,**7** (47), P. 26266–26274.

Submitted 10 June 2022; revised 25 August 2022; accepted 29 August 2022

Information about the authors:

Runjun Sarma – Mehr Chand Mahajan DAV College for Women, Sector 36, Chandigarh, India;
ORCID 0000-0003-4000-7787; runjun2018chd@gmail.com

Munmi Sarma – Former Research Scholar, Sensors & Biosensors group, Autonomous University of Barcelona, Spain; munmisarma11@gmail.com

Manash Jyoti Kashyap – Polymer Technology Consultant, Chandigarh, India; manashjk@gmail.com

Conflict of interest: on behalf of all authors, the corresponding author states that there is no conflict of interest.